8072–8084 *Nucleic Acids Research, 2012, Vol. 40, No. 16* *Published online 19 June 2012*
doi:10.1093/nar/gks510

Structural flexibility of RNA as molecular basis for Hfq chaperone function

Euripedes de Almeida Ribeiro Jr[1], Mads Beich-Frandsen[1], Petr V. Konarev[2], Weifeng Shang[2], Branislav Večerek[3], Georg Kontaxis[1], Hermann Hämmerle[3], Herwig Peterlik[4], Dmitri I. Svergun[2,*], Udo Bläsi[3,*] and Kristina Djinović-Carugo[1,5,*]

[1]Department of Structural and Computational Biology, Max F. Perutz Laboratories, University of Vienna, Campus Vienna Biocenter 5, A-1030 Vienna, Austria, [2]EMBL-Hamburg c/o DESY, Notkestrasse 85, D-22603 Hamburg, Germany, [3]Department of Microbiology, Immunobiology and Genetics, Max F. Perutz Laboratories, University of Vienna, Dr. Bohrgasse 9, A-1030 Vienna, Austria, [4]Faculty of Physics, University of Vienna, Boltzmanngasse 5, A-1090 Vienna, Austria and [5]Department of Biochemistry, Faculty of Chemistry and Chemical Technology, University of Ljubljana, Aškerčeva 5, 1000 Ljubljana, Slovenia

Received February 13, 2012; Revised May 5, 2012; Accepted May 9, 2012

ABSTRACT

In enteric bacteria, many small regulatory RNAs (sRNAs) associate with the RNA chaperone host factor Q (Hfq) and often require the protein for regulation of target mRNAs. Previous studies suggested that the hexameric *Escherichia coli* Hfq (Hfq_{Ec}) binds sRNAs on the proximal site, whereas the distal site has been implicated in Hfq–mRNA interactions. Employing a combination of small angle X-ray scattering, nuclear magnetic resonance and biochemical approaches, we report the structural analysis of a 1:1 complex of Hfq_{Ec} with a 34-nt-long subsequence of a natural substrate sRNA, DsrA ($DsrA_{34}$). This sRNA is involved in post-transcriptional regulation of the *E. coli rpoS* mRNA encoding the stationary phase sigma factor RpoS. The molecular envelopes of Hfq_{Ec} in complex with $DsrA_{34}$ revealed an overall asymmetric shape of the complex in solution with the protein maintaining its doughnut-like structure, whereas the extended $DsrA_{34}$ is flexible and displays an ensemble of different spatial arrangements. These results are discussed in terms of a model, wherein the structural flexibility of RNA ligands bound to Hfq stochastically facilitates base pairing and provides the foundation for the RNA chaperone function inherent to Hfq.

INTRODUCTION

The *Escherichia coli* host factor Q (Hfq) was originally identified as an accessory factor of the phage Qß replicase >40 years ago, whereas its role in bacterial post-transcriptional regulation became evident only more recently (1). Hexameric Hfq protein (protomer: 102 aa) belongs to the class of Sm-like proteins with multiple functions in eukaryotic RNA metabolism (2,3). In bacteria, small regulatory trans-acting RNAs (sRNAs) can modulate different stress responses through post-transcriptional regulation (4). In general, sRNAs either prevent ribosome loading onto the mRNA by base pairing with or in the vicinity of the ribosome binding site or act by an 'anti-antisense' mechanism and abrogate intramolecular inhibitory stem–loop structures that block ribosome binding (5). As many sRNAs display imperfect and non-contiguous target complementary, the requirement for Hfq in riboregulation has mainly been attributed to its RNA chaperone function, which appears to facilitate the interaction between the sRNA and the cognate mRNA (2,6).

Escherichia coli Hfq (Hfq_{Ec}) homologues have been found in a number of Gram-negative and Gram-positive bacteria. The hexameric Hfq proteins possess an evolutionarily conserved common core consisting of amino acid (aa) residues 7–66, whereas there is considerable variation at the C-terminal end (7). Several high-resolution structures of Hfq proteins of different origin bound to

*To whom correspondence should be addressed. Tel: +43 1 4277 52203; Fax: +43 1 4277 9522; Email: Kristina.Djinovic@univie.ac.at
Correspondence may also be addressed to Dmitri I. Svergun. Tel: +49 40 89902 125; Fax: +49 40 89902 149; Email: Svergun@EMBL-Hamburg.de
Correspondence may also be addressed to Udo Bläsi. Tel: +43 1 4277 54609; Fax: +43 1 4277 9546; Email: Udo.Blaesi@univie.ac.at
Present address:
Branislav Večerek, Institute of Microbiology, Academy of Sciences of the Czech Republic, v.v.i., 14220 Prague 4, Czech Republic.

The authors wish it to be known that, in their opinion, the first two authors should be regarded as the joint First authors.

RNA oligonucleotides have been published. The first 3D structure of the 77 aa *Staphylococcus aureus* Hfq protein in complex with the short 5′-AU_5G-3′ oligoribonucleotide revealed that the poly(U) oligonucleotide was bound in a circular fashion along the inner basic rim of the central pore (8). Afterwards, a mutational analysis performed with Hfq_{Ec} further indicated that sRNAs bind to the same site, which was termed the proximal face of the hexamer (9). In addition, the crystal structure of *Salmonella typhimurium* Hfq (protomer: 102 aa) in complex with an $(U)_6$ RNA oligonucleotide not only corroborated poly(U) binding to the proximal side but also revealed that a free 3′ hydroxyl group of RNA is important for high-affinity binding to the protein, which in turn may impact on the stability of RNA substrates (10).

In contrast to uridine-containing sequences, a recent structural study revealed binding of a poly(A) tract to the distal face of Hfq through six tripartite binding motifs (11). Similarly, a crystallographic analysis demonstrated binding of an $A(G)_3A$ aptamer to the distal side of the *Bacillus subtilis* Hfq protein, but the overall RNA structure and protein–RNA interaction patterns differed from those of the Hfq_{Ec}–poly(A) complex (12). Moreover, the crystal structure of a ternary complex between a C-terminally truncated Hfq_{Ec} variant, ADP and an $A(U)_6A$ RNA oligonucleotide derived from the Hfq_{Ec} binding region of the sRNA DsrA (see below) has been recently reported (13). In this structure, the ADP was bound on the distal R site(s) of Hfq_{Ec}, similar to the adenines of poly(A) (11), while the $(U)_6A$ part of the RNA oligonucleotide was bound on the proximal side in a circular fashion, in a manner comparable to $A(U)_6G$ binding to *S. aureus* Hfq (8). Moreover, the 5′ proximal A nucleotide of $A(U)_6A$ was found inserted into a distal R site of another closely packed Hfq hexamer (13).

A paradigm for positive regulation by an sRNA entails the translational activation of *E. coli rpoS* mRNA (Supplementary Figure S1), encoding the stationary phase sigma-factor RpoS, by the sRNA DsrA. At low growth temperatures, the DsrA–*rpoS* mRNA interaction counteracts an inhibitory stem–loop structure that impedes ribosomal access to the ribosome binding site of *rpoS* (14). *In vivo* DsrA–*rpoS* duplex formation at low temperature requires Hfq (15) and the CsdA helicase (16) and creates an RNase III cleavage site within the duplex that would prevent reuse of DsrA (17). DsrA binds to Hfq with a 1:1 stoichiometry (18) on the proximal face (9), whereas *rpoS* mRNA is believed to be recruited on the distal side of Hfq via A-rich element(s) in the mRNA leader (11,19,20). Mechanistic insights into the sequence of events toward Hfq-mediated DsrA–*rpoS* duplex formation have been recently obtained by the Woodson laboratory. Soper *et al.* (6) provided evidence that Hfq increases the stability of the DsrA–*rpoS* complex by binding to the upstream A-rich regions, which is in line with a spectroscopic study (21), indicating that rapid co-binding of two RNA ligands and their release from Hfq precedes duplex formation. The need for Hfq to cycle off its binding site on DsrA before or during annealing with *rpoS* (22) could result from the fact that at least part of the Hfq binding site on DsrA (23) base pairs with *rpoS* mRNA (24). While the dedicated sRNA and mRNA binding surfaces on either site of the Hfq hexamer could readily serve to transiently increase the local concentration of two RNA substrates, the inherent capacity of Hfq to induce conformational changes in RNAs (25–28) could, together with the possibility of several RNA-binding modes within the hexamer, lead to different spatial arrangements of RNA substrates in individual Hfq–RNA complexes, which may in turn increase the likelihood for productive duplex formation.

To address this question, we used small angle X-ray scattering (SAXS), nuclear magnetic resonance (NMR) and biochemical studies together with available information on high-resolution X-ray structures to assess the biophysical parameters and shape of Hfq_{Ec} and a truncated version thereof, Hfq_{Ec65} (aa 1–65), in complex with a 34-nt segment of DsrA domain II ($DsrA_{34}$). Taken together, these data revealed that binding of $DsrA_{34}$ to both the full-length and the truncated protein results in an ensemble of complexes where $DsrA_{34}$ is bound in a structurally variable manner on the proximal face of a given hexamer. These results are discussed in light of the RNA chaperone function of Hfq_{Ec} in riboregulation.

MATERIALS AND METHODS

Synthesis and purification of Hfq_{Ec} and Hfq_{Ec65}

The Hfq proteins used in this study were purified as previously described (29). For NMR experiments, the proteins were uniformly isotope labelled with ^{15}N and ^{13}C.

Enzymatic probing of $DsrA_{34}$ with RNase V1

Aliquots containing 0.15 pmol of [^{32}P]-5′end-labelled $DsrA_{34}$ were incubated in buffer (50 mM bicine pH 8.8, 100 mM NaCl, 250 mM KCl and 0.5 mM $MgCl_2$) in the presence or absence of Hfq_{Ec} (1.5 pmol as hexamer) at 37°C for 10 min. Then, 7.5×10^{-3} (Figure 2B, lanes 2 and 4) and 1.5×10^{-2} (Figure 2B, lanes 3 and 5) units of RNase V1 were added and the incubation at 37°C was continued for 10 min. Then, 2× RNA loading dye was added to stop the reaction. For complete RNA hydrolysis, 0.15 pmol of radioactively labelled $DsrA_{34}$ was incubated at 85°C for 10 min in 50 mM sodium carbonate ($NaHCO_3$/Na_2CO_3), pH 9.0, in the presence of 1 μg yeast tRNA. The RNA hydrolysis was terminated by addition of 1 volume 2× RNA loading dye. The samples were analysed on a 10% polyacrylamide gel containing 8 M urea and the labelled RNA fragments were visualized using a PhosphoImager.

Hfq_{Ec}–$DsrA_{34}$ complex preparation and screening of solution conditions

The $DsrA_{34}$ RNA was chemically synthesized by Thermo Fisher Scientific, Inc., and was further purified on 8% polyacrylamide–8 M urea gels using standard procedures. $DsrA_{34}$ samples were heated to 75°C for 15 min and immediately cooled down on ice, whereas Hfq_{Ec65} was kept at room temperature. Samples were centrifuged for 30 min

at 13 000*g* at room temperature. Before protein–RNA complex assembling, protein and RNA concentrations were determined with a NanoDrop ND-1000 UV/Vis spectrophotometer at 280 and 260 nm, respectively.

To identify suitable conditions for long-term stabilization of Hfq_{Ec65}–$DsrA_{34}$ complexes, a series of sample buffer conditions were screened in 96-well plates (Intelli-Plate 96-3, Art Robbins Instruments, Inc.) containing 1 µl of Hfq_{Ec65} at a final concentration of 3.5 mg/ml in duplicate. These drops were set up using a Phoenix robot (Art Robbins Instruments, Inc.). Upon addition of stoichiometric amounts of $DsrA_{34}$ to Hfq_{Ec65}, the samples were left at room temperature (22°C) and visually examined at time 0 and over the course of 12 h using a Minstrel™ drop imager (Rigaku Americas Corporation). The drops without visible precipitation (14 conditions out of 96) were analysed by dynamic laser light scattering (DLS) experiment. The best four candidate conditions were selected on the basis of the lowest polydispersity index (PdI) derived from the DLS experiment. Then, a time course at different temperatures was performed using DLS to monitor the condition and the time point where the Hfq_{Ec65}–$DsrA_{34}$ complex samples acquired a PdI ≤ 15%. A long-term stability and monodispersity of Hfq_{Ec}–$DsrA_{34}$ and Hfq_{Ec65}–$DsrA_{34}$ complexes were achieved in 50 mM phosphate buffer, pH 7.2, containing 200 mM NaCl and in 50 mM bicine buffer, pH 8.8, containing 100 mM NaCl and 250 mM KCl.

Dynamic laser light scattering

Typically, samples with protein concentration ranging from 1 to 10 mg/ml were centrifuged 30 min at 13 000*g* to eliminate large aggregates. DLS was measured at a scattering angle of 90° on a DynaProNanoStar™ (Wyatt Technology) using a 10 µl microcuvette and a laser emitting at $\lambda = 662$ nm. The data collection was conducted with laser intensity in autoregulation mode, using 10 acquisition frames of 10 s/acquisition at 25 or 35°C. The data were analysed using online Wyatt software to determine the sample PdI, where sample with an average PdI ≤ 15% was considered as monodisperse and suitable for structural characterization. The apparent translational diffusion coefficient, *D*, calculated from the intensity autocorrelation functions fits, was converted into Stokes radii (R_s) according to the Stokes–Einstein equation (Eq. (1)):

$$R_s = \frac{RT}{N6\pi nD} \quad (1)$$

with *R* being the gas constant, *T* the temperature, *N* Avogadro's number and *n* the solvent viscosity. Control experiments carried out with Hfq_{Ec} and Hfq_{Ec65} alone yielded experimental Stokes radii similar to the ones computed from atomic coordinates of rigid structures by the program HYDROPRO (30) that employs shell-model methodology. In this calculation, the crystal structure of *E. coli* Hfq (PDB accession code: 1HK9) (7) was used as the structural (PBD) file for Hfq_{Ec65}, while the SAXS model described by Beich-Frandsen *et al.* (29) was employed for the Hfq_{Ec}. The primary solution property derived here was translational diffusion coefficient (*D*) that was converted into Stokes radii (R_s) according to Eq. (1). For running HYDROPRO, the radius of the atomic elements (AER) was defined to be 2.9 Å. The number of values of the radius of the mini bead (NSIG) was set to be 6, and the radius of the mini beads in the shell was set to 2.0 for SIGMIN and 3.0 for SIGMAX. The solvent viscosity was defined to be 0.0200 poise. Partial specific volume (psv) for protein alone was set to be 0.732 cm^3/g, while for Hfq_{Ec}–$DsrA_{34}$ and Hfq_{Ec65}–$DsrA_{34}$ complexes, the psv values were calculated to be 0.706 and 0.696 cm^3/g according to the relative contribution of the pvs of RNA $DsrA_{34}$ (0.550 cm^3/g) in these respective protein–RNA complexes at stoichiometric ratio (1:1). The structural PDB files for the complexes were obtained from the SAXS models. The temperature was defined to be 298 or 308 K.

Nuclear magnetic resonance

For the NMR experiments, the complexes were prepared between unlabelled RNA and doubly $^{15}N/^{13}C$ isotope-labelled protein. All NMR experiments were performed at 37°C with a Varian Inova 600 MHz spectrometer and with a Varian Inova 800 MHz spectrometer. Before data collection, the Hfq_{Ec65}–$DsrA_{34}$ complex samples were incubated overnight to optimize the sample monodispersity level as suggested by the DLS experiment (Supplementary Figure S3). NMR spectra were processed with NMRPipe (31) and analysed with Sparky (32) software. The protein samples for the NMR experiments were prepared by size-exclusion chromatography in 50 mM Na_3PO_4, pH 7.2, 200 mM NaCl and concentrated to ~1 mM Hfq_{Ec65} (with respect to the monomer). Samples were supplemented with 10% (vol/vol) D_2O to provide the deuterium signal for the field-frequency lock, as well as 0.1–0.2% (wt/vol) NaN_3 to inhibit bacterial growth. 1D ^{1}H-NMR spectra were obtained using the WATERGATE (33) method for solvent suppression. Backbone signal assignment for the C-terminally truncated mutant Hfq_{Ec65} was obtained by a suite of standard (sensitivity enhanced) 3D triple resonance experiments: HNCA (34), HN (CO)CA (35), HNCACB (36) and HNCO (34) were recorded for sequential backbone chemical shift assignment of Hfq_{Ec65} as described by Beich-Frandsen *et al.* (29). ^{15}N relaxation times (T_1, T_2) were measured using gradient sensitivity-enhanced 2D methods with ^{1}H detection (37,38). Sequential backbone signal assignments in the apo form were available for Hfq_{Ec65} for aa residues 6–65 (29) and were used as starting points for signal assignment for the Hfq_{Ec65}–$DsrA_{34}$ complex. The fingerprint region of the ^{15}N-HSQC spectra of Hfq_{Ec65} was superimposed onto the ^{15}N-HSQC spectra of the Hfq_{Ec65}–$DsrA_{34}$ complex (Figure 1A). Both spectra were well resolved and largely similar, which allowed for sequential assignment of most of the resonances of the Hfq_{Ec65}–$DsrA_{34}$ complex spectra by simple peak comparison. The remainder of backbone signal assignment of the complex between Hfq_{Ec65} and $DsrA_{34}$ was obtained employing HNCA (34)/HN(CO)CA (35) and HNCO (34) experiments. When necessary, ambiguous ^{1}H–^{15}N assignments of the

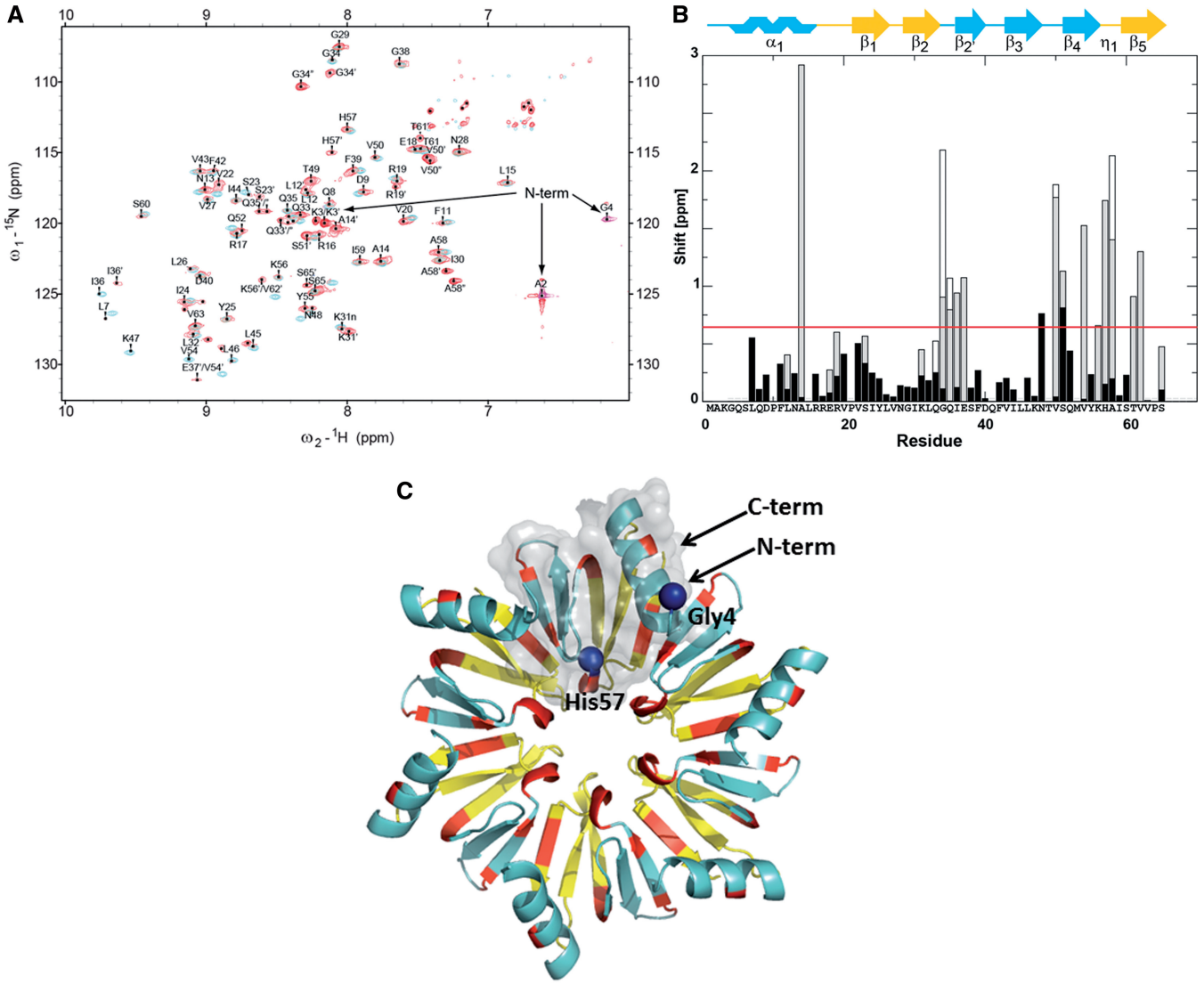

Figure 1. NMR analysis of the Hfq_{Ec65}–$DsrA_{34}$ complex. (**A**) ^{13}C-, ^{15}N-labelled Hfq_{Ec65} was used for solution NMR studies. Assignments are indicated for the complex Hfq_{Ec65}–$DsrA_{34}$. Superposition of the ^{1}H–^{15}N HSQC spectra of Hfq_{Ec65} RNA free form (blue) and in complex with $DsrA_{34}$ (red). (**B**) Chemical ^{1}H–^{15}N shift differences between Hfq_{Ec65} and Hfq_{Ec65}–$DsrA_{34}$ complex (calculated as $\mathrm{sqrt}(\Delta^{15}N^2 + 25\Delta^{1}H^2)$ for assigned peaks plotted against residue positions. Multiple sets of signals observed for certain residues are indicated in grey (two signals) and white (three signals), respectively. The Hfq_{Ec65} secondary structure is indicated and colour coded according to the position on the proximal (blue) and distal face (yellow). The distal and proximal portion of the β2-strand are termed β2 and β2′, respectively; η1 denotes the small 3_{10}-helix. The red line indicates the chemical shift differences threshold (double the average shift change) above which the chemical shift differences were considered significant. (**C**) Ribbon diagram of Hfq_{Ec65} hexamer. Residues with prominent chemical shift differences are colour coded in red and mapped onto the 3D structure of Hfq_{Ec65} derived from the crystal structure pdb1HK9 (7); residues belonging to proximal and distal sites are colour coded as in (B). Residues Gly4 and His57, used in SAXS modelling as contact points with $DrsA_{34}$, are presented as blue spheres. Semitransparent solvent accessible surface of one Hfq_{Ec65} protomer is displayed in grey.

Hfq_{Ec65}–$DsrA_{34}$ complex were resolved by inspection of their attached $^{13}C\alpha$ or $^{13}C'$ shifts.

SAXS, ab initio shape determination and molecular modelling

SAXS experiments were performed at the EMBL BioSAXS beamline X33 (39,40) at the DORIS III synchrotron storage ring (DESY, Hamburg, Germany). A1M PILATUS detector (DECTRIS, Switzerland) was installed at a sample-to-detector distance of 2.7 m. At the X-ray wavelength $\lambda = 1.5$ Å, this beamline setup records the scattering profiles in the range of momentum transfers between 0.01 and 0.6 $Å^{-1}$ ($s = 4\pi \sin\theta/\lambda$, where 2θ is the scattering angle). The data reduction and analysis followed the standard procedures using the ATSAS program package (41). All samples were in 50 mM bicine buffer, pH 8.8, containing 100 mM NaCl and 250 mM KCl and the measurements were performed at 35°C. Hfq_{Ec} alone was measured at concentrations 4.1 and 15 mg/ml; the complex Hfq_{Ec}–$DsrA_{34}$ was measured at 2.3, 4.3 and 9.2 mg/ml, while Hfq_{Ec65} alone was measured at 2.5, 3.8 and 9.4 mg/ml and the complex

Hfq_{Ec65}–$DsrA_{34}$ at 2.6, 4.0 and 5.1 mg/ml. The protein concentrations were determined with a Nanodrop ND-1000 UV/Vis spectrophotometer at 280 nm immediately before X-ray exposure.

Overall parameters, i.e. the forward scattered intensity $I(0)$, radius of gyration R_g and the excluded volume of the particles, were calculated using PRIMUS (42). The program GNOM (43) was employed for calculating the pair distance distribution function and to estimate the maximum dimension (D_{max}) of the particle. No concentration dependence was found for the Hfq_{Ec65}–$DsrA_{34}$ complex, whereas a continuous increase of overall parameters for Hfq_{Ec}–$DsrA_{34}$ complex was observed. For further analysis, the data from the lowest concentration of complexes, compatible with 1:1 stoichiometry of the complex, were used. The low-resolution shapes were reconstructed *ab initio* using the program DAMMIN (44).

To assess the flexibility of $DsrA_{34}$ in the complexes, the ensemble optimization method (EOM) was used (45). A random pool of 10 000 models for the Hfq_{Ec}–$DsrA_{34}$ complex was generated from the atomic coordinates of Hfq_{Ec} (29) and a chain of dummy residues representing the RNA molecule using RanCh (45). As the scattering density of a nucleotide is about 2.8 times larger than that of an aa residue, and as the volume of a nucleotide is two times larger than the volume of an aa residue, 136 dummy residues with the form-factor multiplier equal to one were used to represent $DsrA_{34}$. This approach enables EOM to emulate flexible RNA moieties for the Hfq_{Ec}–$DsrA_{34}$ complex. A subset of the ensemble was selected using a genetic algorithm such that the calculated scattering of the mixture agreed with the experimental data. The R_g distributions of the selected ensembles were obtained by repeating the selection process multiple times. To better account for the relative difference in scattering density between RNA and protein, we generated a full-atom model of $DsrA_{34}$ in unfolded conformation. This model on one hand was used to simulate a scattering profile of $DsrA_{34}$ and on the other allowed us to validate the stoichiometry of the complexes and to estimate the effective difference in scattering density between the Hfq_{Ec}–$DsrA_{34}$ complex and Hfq_{Ec}.

Finally, the rigid body modelling of the protein–RNA complexes was done using the program SASREF (46). To model $DsrA_{34}$ in the complexes, a tentative 3D model was generated using the programme package RNABuilder (47,48) and subsequently divided into six fragments, in agreement with the persistency length of one unfolded single RNA molecule (49,50), generating in this way a chain of interconnected rigid subunits. Contacts were defined to guarantee the interactions of $DsrA_{34}$ on the proximal face of Hfq hexamer, with the poly(U) stretch (Supplementary Figure S2) interacting with one of the 'YKH' motifs, while the next three nucleotides contact aa residues 2–4 of Hfq, as suggested by the NMR studies (Figure 1A–C). In the case of Hfq_{Ec65}–$DsrA_{34}$, the crystal structure of *E. coli* Hfq (PDB accession code: 1HK9) (7) was used as the rigid subunit, while the model described by Beich-Frandsen *et al.* (29) was used for the Hfq_{Ec}–$DsrA_{34}$ complex.

RESULTS

Hydrodynamic properties of Hfq–DsrA complexes assessed by DLS

The protein–RNA complexes were formed between Hfq_{Ec} or Hfq_{Ec65} and a 34-nt fragment of DsrA (Supplementary Figure S2), spanning DsrA domain II (23). Binding of $DsrA_{34}$ to both Hfq_{Ec} and Hfq_{Ec65} was confirmed by electrophoretic mobility shift assays (not shown). DLS was used to determine the PdI and the Stokes' radii (R_s) of both complexes (Supplementary Figure S3). Samples with average PdI values $\leq$15% were considered monodisperse and suitable for structural characterization. A long-term stability and monodispersity of Hfq_{Ec}–$DsrA_{34}$ and Hfq_{Ec65}–$DsrA_{34}$ complexes were achieved in 50 mM phosphate buffer, pH 7.2, containing 200 mM NaCl and in 50 mM bicine buffer, pH 8.8, containing 100 mM NaCl and 250 mM KCl. The DLS experiments revealed that the Hfq_{Ec}–$DsrA_{34}$ complex is monodisperse up to a final concentration of 3 mg/ml and displayed an R_s of 46 ± 1 Å, whereas the R_s for Hfq_{Ec} alone was 35 ± 2 Å. The Hfq_{Ec65}–$DsrA_{34}$ complex showed monodispersity up to 9 mg/ml with an R_s of 37 ± 2 Å, whereas that of free Hfq_{Ec65} was 30 ± 2 Å. Furthermore, global analysis of the DLS autocorrelation functions (Supplementary Figure S3) corroborated the monodispersity of the complex assembled at 1:1 stoichiometry for the samples used for NMR and SAXS experiments.

NMR indicates binding of $DsrA_{34}$ to the proximal face of the Hfq hexamer with 1:1 stoichiometry

NMR was used to gain more information on the structural and dynamic properties of the Hfq_{Ec65}–$DsrA_{34}$ complex in solution. The complex is in a 'slow exchange situation' reflecting the high affinity of $DsrA_{34}$ for Hfq_{Ec65}. Binding of the RNA to the symmetrical hexameric Hfq_{Ec65} changed the appearance of the NMR spectra. Upon the interaction with $DsrA_{34}$, the original 6-fold symmetry of the Hfq_{Ec65} hexamer is broken and additional sets of cross-peaks, corresponding to the different subunits of the Hfq_{Ec65} hexamer, started to emerge in the ^{15}N-HSQC spectra (Figure 1A). In theory, all the individual subunits of Hfq_{Ec65} are non-equivalent. However, in practice, only some of the subunit residues in direct contact with RNA experience significant shifts relative to apo-Hfq_{Ec65}. Typically, only two or in very few cases three sets of signals were detected for a number of residues. This is compatible with a binding mode in which the $DsrA_{34}$ predominantly interacts with one protomer of the hexameric Hfq_{Ec65}. Due to the high affinity (nM) of the Hfq_{Ec65}–$DsrA_{34}$ interaction, no exchange between the different non-equivalent species could be detected by NMR. When compared with Hfq_{Ec65} alone, significant ^{15}N–$^{1}H^{N}$ chemical shift differences between the signal sets of the interacting and non-interacting subunits were observed in the Hfq_{Ec65}–$DsrA_{34}$ complex in the N-terminal α-helix, in β-strand β2′, in the proximity of the central pore, within the central pore that comprises the YKH motif (aa 55–57) and in the C-terminal β-strand β5 (Figure 1B and C).

The YKH motif of *S. aureus* Hfq was shown to interact with poly-U (8) and is anticipated to serve as the primary binding site for sRNAs in Hfq_{Ec} (9). In addition, upon complex formation with $DsrA_{34}$, the amino acids A2–G4 of the partially disordered N-terminus (29) became apparently conformationally stabilized and thus detectable. As anticipated for close contacts with aromatic nucleobases, high upfield ^{15}N shifts [~95 (folded to 125) ppm for residue 2 and ~90 (folded to 120) ppm for residue 4] were observed (Figure 1A). Hence, the proximal side residues A2 and G4 are apparently in contact with RNA.

Besides the N-terminus, a number of clusters of significant ^{15}N–$^{1}H^{N}$ chemical shift changes were identified. One large ^{15}N–$^{1}H^{N}$ chemical shift change maps to residue Ala14, residing in the central region of the N-terminal α-helix on its solvent-exposed side (Figure 1B and C). Ala14 could sense the conformational changes at the N-cap of the α-helix, caused by RNA interacting with the N-terminal aa residues 2–4. As expected, the YKH motif with a shell of surrounding residues experiences a difference in chemical environment upon binding of $DsrA_{34}$ (Figure 1B and C). The third group of notable chemical shifts locates to the outer rim of the Hfq hexamer, i.e. to aa residues 34–37, in a conformationally labile region at the end of the β2-strand and turn connecting to the following β2′-strand (Figure 1B and C). In summary, the chemical shift analyses suggested that the RNA is bound to the central pore and that it emerges from the proximal side, tethered by interactions with the N-terminal aa residues 2–4, which precede the α1-helix on the proximal side and point toward the central pore (Figure 1B and C). In support, the Hfq_{EcK31A} mutant protein, which was shown to be strongly impaired in poly(A) binding to the distal site (51), was not impaired in binding to $DsrA_{34}$, corroborating the chemical shift analyses (not shown).

The effect of adenine binding in the distal R binding site was independently investigated by titration with ATP (not shown). This ruled out simultaneous binding of $DsrA_{34}$ to both the proximal and the distal side of Hfq_{Ec} and a 2:1 stoichiometry as observed in complex with the RNA molecules used in the study by Wang *et al.* (13). This different behaviour can be best rationalized by the lack of a 5′ terminal A in our $DsrA_{34}$ construct, which is obviously required for binding to the distal side (11).

Next, the ^{15}N relaxation rates were measured to obtain information on the hydrodynamic radius, thus the effective molecular mass and consequently on the stoichiometry of the Hfq_{Ec65}–$DsrA_{34}$ complex. The NMR ^{15}N relaxation measurements revealed for Hfq_{Ec65} (43.2 kDa) a $T_2 = 40.0 \pm 2.1$ ms ($R_2 = 25.0 \pm 1.3\,s^{-1}$) at 14.1 T (i.e. 600 MHz ^{1}H frequency). For the Hfq_{Ec65}–$DsrA_{34}$ complex (50.5 kDa), T_2 was determined with 29.0 ± 6.5 ms ($R_2 = 34.5 \pm 7.7\,s^{-1}$) at the same field strength for the signals of the core region. This agreed with the molecular weight increase expected for a 1:1 stoichiometry between Hfq_{Ec65} and $DsrA_{34}$. Thus, the NMR studies strongly suggested that under these conditions, complex formation predominantly occurs in a 1:1 ratio. Moreover, no imino ^{1}H resonances indicative of stable base pairs in double-stranded nucleic acids, which are observable in the 1D ^{1}H NMR spectra of free $DsrA_{34}$, were detected in the 1D ^{1}H NMR spectra of the Hfq_{Ec65}–$DsrA_{34}$ complex (Figure 2A). The lack of stable base pairing in the Hfq_{Ec65}–$DsrA_{34}$ complex suggested an extended and single-stranded conformation of $DsrA_{34}$, where the imino ^{1}Hs are prone to solvent exchange in the absence of base pairing. Similarly, the H_3 imino Hs of the poly U tract at the 5′-end of $DsrA_{34}$, which are expected to be bound to the central pore of Hfq_{Ec65} (similar to A(U)6G binding to *S. aureus* Hfq (8)), are outward-facing towards the solvent and thus not expected to yield observable signals. To obtain additional experimental support for an extended conformation of DsrA bound to Hfq, enzymatic probing with the double-stand specific endoribonuclease V1 was performed. This analysis revealed that the stem–loop structure in $DsrA_{34}$ is at least partially formed in the absence of Hfq, whereas no indications for base pairing were obtained when a 1:1 complex of Hfq_{Ec65} hexamer and $DsrA_{34}$ was treated with the enzyme (Figure 2B–D). These chemical probing experiments are in agreement with a FRET study by Večerek *et al.* (28), showing that both Hfq_{Ec} and Hfq_{Ec65} induce structural changes in full-length DsrA.

Low-resolution shape of Hfq_{Ec65}–$DsrA_{34}$ and Hfq_{Ec}–$DsrA_{34}$complexes

SAXS measurements were performed in parallel with the complexes Hfq_{Ec}–$DsrA_{34}$ and Hfq_{Ec65}–$DsrA_{34}$ at three different sample concentrations (Hfq_{Ec}–$DsrA_{34}$: 2.3, 4.3 and 9.2 mg/ml and Hfq_{Ec65}–$DsrA_{34}$: 2.6, 4.0 and 5.1 mg/ml). To avoid aggregation or concentration-induced artefacts, we used only the lowest concentrations of both complexes, corresponding to a 1:1 stoichiometry, which is in agreement with a study by Updegrove *et al.* (18) who reported that DsrA domain II and Hfq_{Ec} form 1:1 complexes.

The processed experimental data are presented in Figure 3A and the overall molecular parameters are summarized in Table 1. The data recorded for Hfq_{Ec} and Hfq_{Ec65} are fully compatible with the results obtained by Beich-Frandsen *et al.* (29). The calculated scattering profile of the crystal structure of Hfq_{Ec65} (PDB accession code: 1HK9) (7) agreed with the experimental SAXS data with a discrepancy $\chi = 1.06$ (Figure 3A), indicating that Hfq_{Ec65} forms a stable hexamer in solution and that the doughnut shape of the crystal structure is retained. For the full-length protein, the model described by Beich-Frandsen *et al.* (29), where the C-terminal regions stretch outward from the central core, also agreed with the present experimental data ($\chi = 1.65$; Figure 3A). The models generated by Beich-Frandsen *et al.* (29) were therefore used in the subsequent analysis of the Hfq_{Ec}–$DsrA_{34}$ and Hfq_{Ec65}–$DsrA_{34}$ complexes.

As shown in Figure 3B, the distance distribution function $P(r)$ of the Hfq_{Ec}–$DsrA_{34}$ complex revealed a skewed appearance typical for an elongated particle. The significant increase in R_g and D_{max} after binding of $DsrA_{34}$ again suggested that the 34-nt RNA molecule is fully extended after binding to the protein. The observed R_g

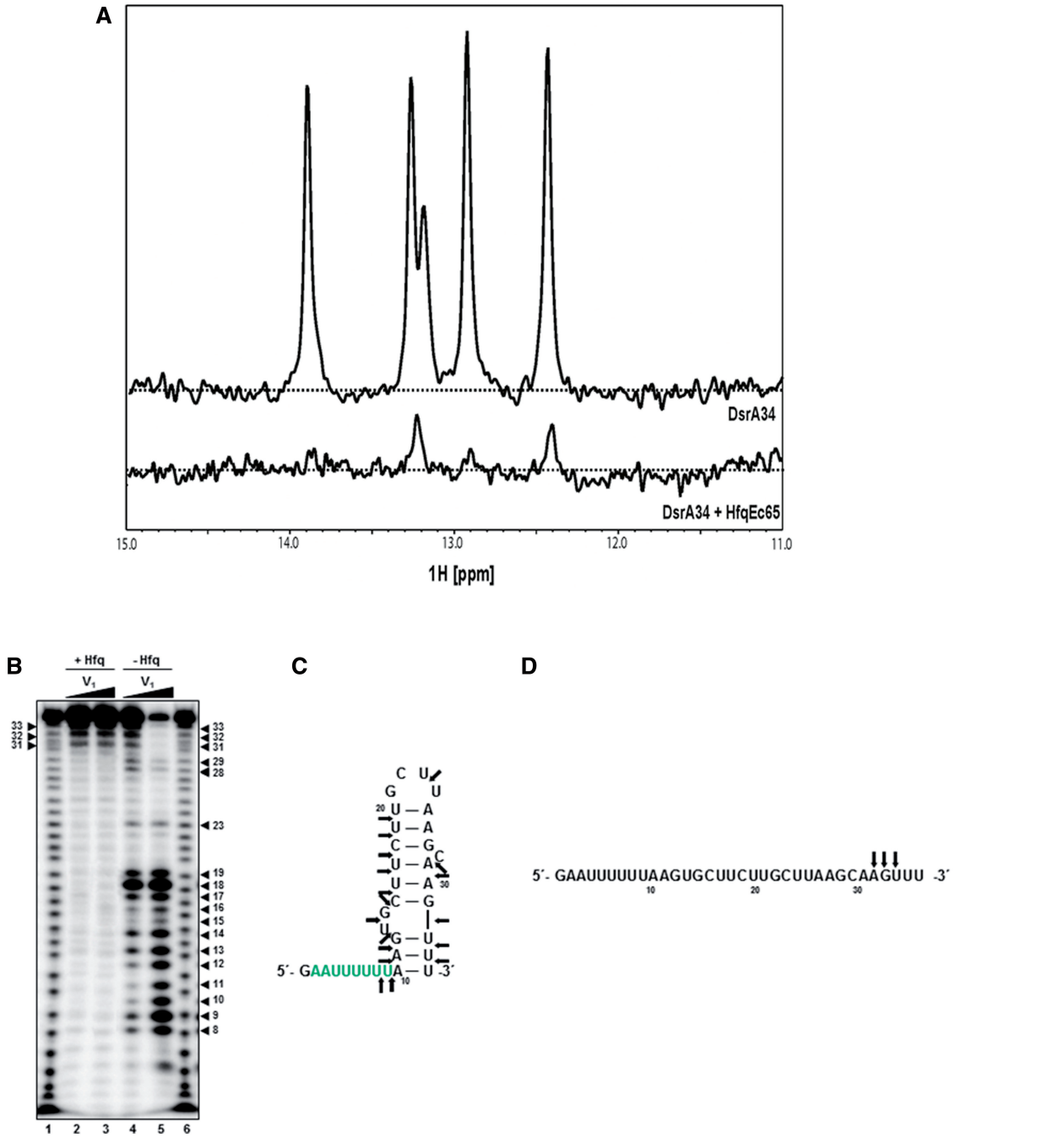

Figure 2. NMR spectra of $DrsA_{34}$ and enzymatic probing of $DsrA_{34}$ with RNase V1 in the presence and absence of Hfq_{Ec}, respectively. (**A**) NMR spectra of free $DrsA_{34}$ and in complex with Hfq_{Ec65}. (**B**) *In vitro* RNase V1 cleavage of $DsrA_{34}$ was performed in the presence (lanes 2 and 3) and in the absence (lanes 4 and 5) of Hfq_{Ec}. 7.5×10^{-3} (lanes 2 and 4) and 1.5×10^{-2} (lanes 3 and 5) units of RNase V1 were added. Lanes 1 and 6, sequence ladder obtained by alkaline hydrolysis of [^{32}P]-5′ end-labelled $DsrA_{34}$. The numbers denote nucleotide positions in $DsrA_{34}$. The arrows denote RNase V1 cleavage sites on $DsrA_{34}$ in the absence (**C**) and presence (**D**) of Hfq_{Ec}, respectively, derived from enzymatic probing.

and D_{max} are incompatible with the presence of a stable stem–loop and can thus be explained by flexible and disordered single-stranded RNA (possibly in a fast exchange equilibrium with other loosely base-paired species). For Hfq_{Ec65} and the Hfq_{Ec65}–$DsrA_{34}$ complex, the changes in R_g and D_{max} follow the same pattern as observed for Hfq_{Ec} and the Hfq_{Ec}–$DsrA_{34}$ complex. The fact that truncation of the C-terminus did not change the behaviour of $DsrA_{34}$ binding and that Hfq_{Ec65} was previously shown to be proficient in DsrA binding (28) suggested that C-terminal residues are not involved in Hfq–$DsrA_{34}$ interactions.

To obtain direct information on the structural changes upon RNA binding, low-resolution *ab initio* models (~25 Å) were reconstructed from the SAXS data. The model of Hfq_{Ec65}–$DsrA_{34}$ shows an elongated particle

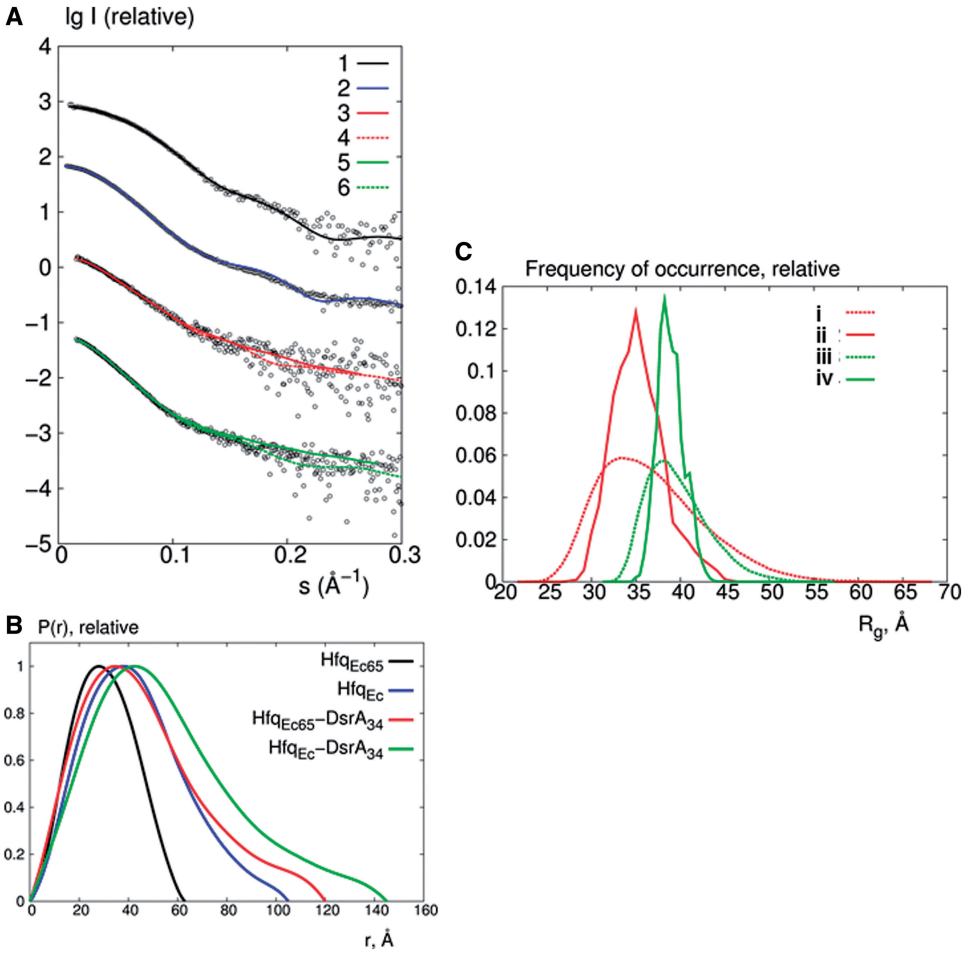

Figure 3. Analysis of the SAXS data. (**A**) Comparison of the experimental SAXS curves (empty circles) with the CRYSOL calculated scattering curves for Hfq_{Ec65} (curve 1) and Hfq_{Ec} (curve 2) using the crystal structure pdb1HK9 (7) and the model reported by Beich-Frandsen *et al.* (29). Typical fits of the *ab initio* models (curves 3 and 5) and rigid body models (curves 4 and 6) against the experimental data for Hfq_{Ec65}–$DsrA_{34}$ (fits with red lines) and Hfq_{Ec}–$DsrA_{34}$ (fits with green lines) complexes, respectively. (**B**) Comparison of the pair distance distribution functions for Hfq_{Ec} and Hfq_{Ec65} alone and the corresponding complexes with $DsrA_{34}$. (**C**) Frequency distributions of R_g obtained in EOM to assess the flexibility of $DsrA_{34}$ in complex with Hfq_{Ec65} (red) and Hfq_{Ec} (green). Dashed curves (i) and (iii) correspond to the distributions for the random pool of 10 000 conformers and curves (ii) and (iv) to the distributions for the optimized ensembles.

Table 1. SAXS parameters calculated from experimental data compared with Stokes radii from DLS experiment and with Stokes radii calculated from the *ab initio* models using the program HYDROPRO (30)

Sample	R_g [SAXS] (Å)	D_{max} [SAXS] (Å)	R_s [DLS] (Å)	R_s [HYDROPRO] *ab initio* model (Å)
Hfq_{Ec}	34 ± 1	105 ± 5	35 ± 2	36
Hfq_{Ec}–$DsrA_{34}$	44 ± 2	145 ± 10	46 ± 1	48
Hfq_{Ec65}	23 ± 1	63 ± 3	30 ± 2	30
Hfq_{Ec65}–$DsrA_{34}$	33 ± 2	120 ± 8	37 ± 2	38

consisting of a bulk region with an extended arm. The crystal structure of Hfq_{Ec} (aa 1–71; PDB accession code: 1HK9) (7) can be docked into the bulk part of the model and the arm, apparently consisting of $DsrA_{34}$, is stretching outward (Figure 4A–C). The elongated *ab initio* model for the complex is further supported by the agreement of a Stokes radius of 38 Å determined from this model by the program HYDROPRO (30) with the measured value (37 ± 2 Å) using DLS (Table 1). Similarly, the model for the Hfq_{Ec}–$DsrA_{34}$ complex displays an arm protruding outwards the protein part represented by the crystal structure of Hfq_{Ec} with the C-terminal residues added as in (29) (Figure 4D–F).

Flexible arrangements of $DsrA_{34}$ in both complexes

As the NMR, SAXS and enzymatic probing studies suggested that $DsrA_{34}$ is unfolded, extended and lacks defined secondary structure when bound to Hfq_{Ec} and Hfq_{Ec65}, the EOM (45) approach was used to assess the flexibility and the accessible conformational space of the complexes. EOM takes into account flexibility by allowing for the coexistence of different conformations of the complex in the population of molecules in solution, contributing to the experimental scattering pattern. In EOM, a large pool

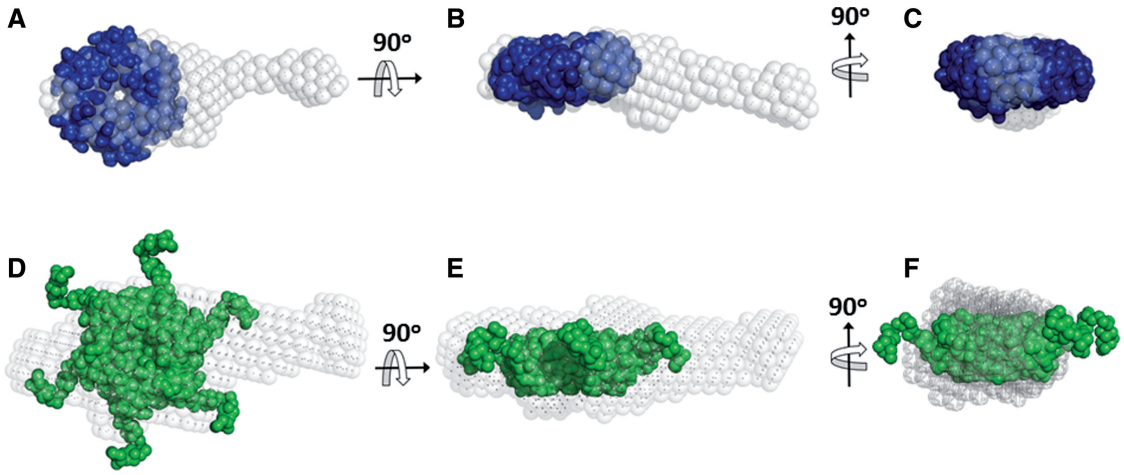

Figure 4. *Ab initio* models of Hfq_{Ec65}–$DsrA_{34}$ and Hfq_{Ec}–$DsrA_{34}$ derived from the SAXS data. (**A–C**) Models of Hfq_{Ec65} (blue) and (**D–F**) Hfq_{Ec} (green) represented with their respective solvent accessible surfaces were docked manually into the bulk region of the *ab initio* shapes. The Hfq_{Ec65} atomic coordinates were derived from the crystal structure pdb1HK9 (7). The Hfq_{Ec} structure was derived from the same atomic coordinates with the C-terminal segment modelled using SAXS data (29).

of random configurations was generated and ensembles were selected from this pool using a genetic algorithm, such that the average computed scattering over the ensemble fitted the experimental scattering data. As shown in Figure 3C, the R_g distributions of the random pools for both samples are rather broad, whereas the selected ensembles both for Hfq_{Ec}–$DsrA_{34}$ and Hfq_{Ec65}–$DsrA_{34}$ display relatively narrow distributions, where the most compact and most extended configurations are not present. The EOM ensembles fitted the scattering data rather well, with a discrepancy χ of 1.3 and 1.0 for Hfq_{Ec}–$DsrA_{34}$ and Hfq_{Ec65}–$DsrA_{34}$, respectively (fits not shown). This indicated that a confined range of conformationally variable Hfq_{Ec65}–$DsrA_{34}$ and Hfq_{Ec}–$DsrA_{34}$ complexes exists in solution. The major insight from EOM was that $DsrA_{34}$ in the complex is unfolded, as the experimental data could not be fitted by compact RNA structures.

The confined flexibility of the complexes permitted rigid body modelling against the SAXS data to visualize the spatial arrangement of $DsrA_{34}$ relative to the hexameric core of the protein. As shown in Figure 3A, the rigid body models generated by SASREF (46) agreed with the experimental data with a typical discrepancy $\chi = 1.2$ for Hfq_{Ec}–$DsrA_{34}$ and $\chi = 1.1$ for Hfq_{Ec65}–$DsrA_{34}$. Ten superimposed independently constructed rigid body models for Hfq_{Ec}–$DsrA_{34}$ and Hfq_{Ec65}–$DsrA_{34}$ revealed that in both complexes the RNA extends like an arm away from the hexamer core, thus leading to an elongated shape. The orientation and the contour length of the RNA arms may vary such that $DsrA_{34}$ explores a manifold of configurations around the core (Figure 5). The obtained conformational space of the RNA molecule is confined to the proximal side of the hexamer, in agreement with the EOM results.

The theoretical Stokes radii (R_s) calculated for the Hfq_{Ec}–$DsrA_{34}$ and Hfq_{Ec65}–$DsrA_{34}$ complexes are equivalent to the R_s derived experimentally from the DLS data (Table 1) and agree with $DsrA_{34}$ binding to Hfq_{Ec} and to Hfq_{Ec65} in extended conformation with a 1:1 stoichiometry. Moreover, the RNA does not interact with the C-terminus of Hfq_{Ec} (Figure 5D–F), suggesting that the C-terminal region of Hfq_{Ec} may not affect the overall conformation of $DsrA_{34}$ and *vice versa*. These results corroborated previous synchrotron radiation circular dichroismn spectroscopy studies, which revealed that $DsrA_{34}$ did not alter the structure of Hfq_{Ec} (29). In contrast, the presence of a longer RNA fragment comprising the 5′ upstream region and the immediate coding region of the *hfq* gene, which was shown to require the C-terminal extension of Hfq_{Ec} for binding (28), did lead to an ordering of the C-terminus of Hfq_{Ec} (29).

DISCUSSION

We used complementary biophysical and structural biology methods to study the arrangement of domain II of the sRNA DsrA on the surface of the Hfq_{Ec} hexamer at a stoichiometry ratio as reported by Updegrove *et al.* (18). Previous electrophoretic mobility shift experiments (22) showed that Hfq can bind to full-length DsrA with a 2:1 ratio, although binding of a second Hfq hexamer required high concentrations of the protein. In addition, a recent biophysical study indicated likewise a 2:1 ratio between Hfq and DsrA (13). Moreover, crystallographic studies by Wang *et al.* (13) revealed that a short oligonucleotide $A(U)_6A$ was bound with the $(U)_6A$ segment to the proximal side of one Hfq hexamer, whereas the 5′A nucleotide was found inserted into a distal R site of a second Hfq hexamer. In our study, the increase of SAXS overall parameters for Hfq_{Ec}–$DsrA_{34}$ at higher concentrations could be explained by the formation of 2:1 (or 2:2) Hfq_{Ec}–$DsrA_{34}$ complexes, which would be in agreement with (13). As no concentration effects were observed for the Hfq_{Ec65}–$DsrA_{34}$ complex (Supplementary Table S1), this interaction is probably not RNA mediated and therefore could occur through interactions of C-terminal residues of Hfq_{Ec}. However, given that Hfq appears to

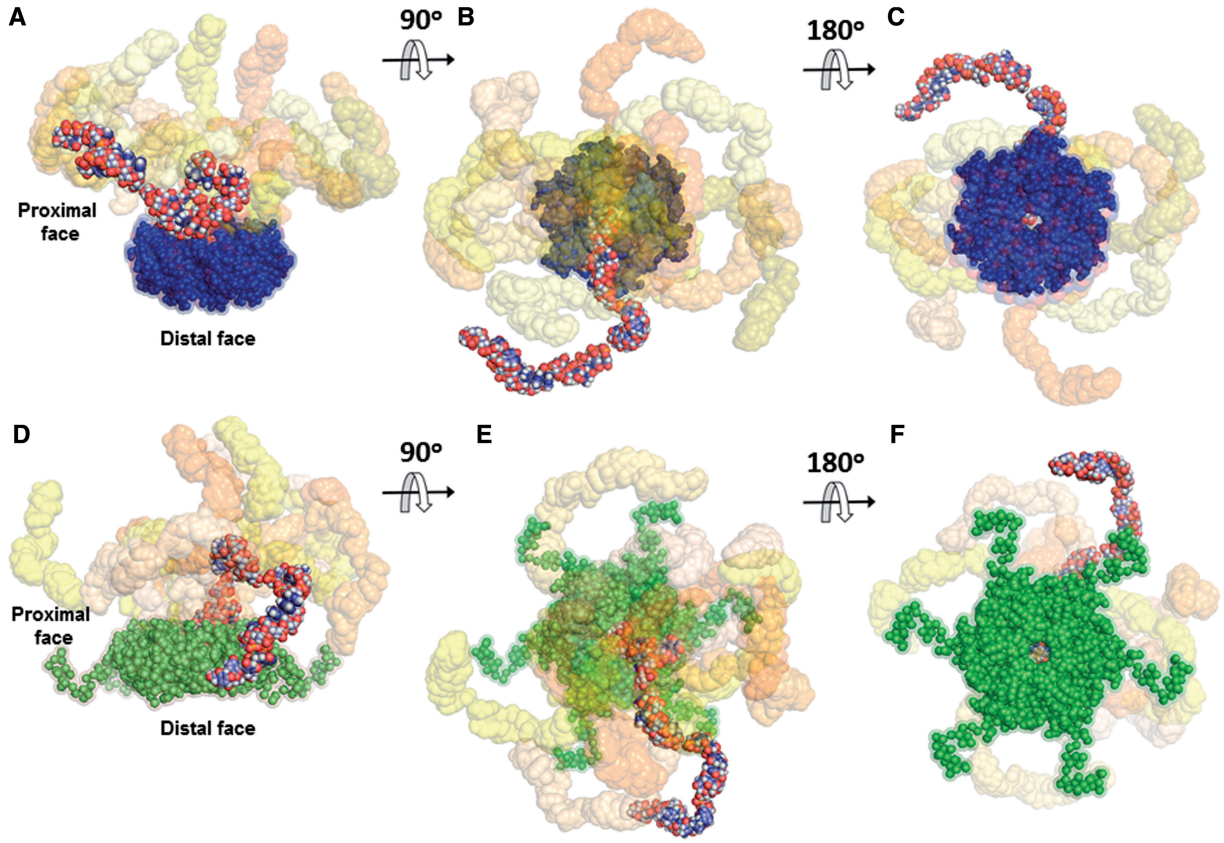

Figure 5. Rigid body models of Hfq_{Ec65}–$DsrA_{34}$ and Hfq_{Ec}–$DsrA_{34}$ complexes. (**A–C**) Ten typical models for the Hfq_{Ec65}–$DsrA_{34}$ complex are superimposed and shown at three different plane rotations. Hfq_{Ec65} atomic coordinates were derived from the crystal structure pdb1HK9 (7) (solvent accessible surface representation in blue). The models were generated using SASREF (46) and SAXS data combined with constraints obtained from NMR. (**D–F**) Ten typical models of the Hfq_{Ec}–$DsrA_{34}$ complex are superimposed and shown at three different plane rotations. The Hfq_{Ec} structure (solvent accessible surface representation in green) was derived from the high-resolution crystal structure pdb1HK9 (7) with the C-terminal segment modelled using SAXS data (29). In both complexes, one $DsrA_{34}$ molecule is represented as full-atom model with atoms colour-coded to highlight the overall structure of the RNA in the complex, while the other nine models are presented with their solvent accessible surface (in different tonalities ranging from light yellow to deep orange). In both cases, the best $DsrA_{34}$ models that fit the SAXS data display an extended conformation. The average root mean square deviation between the $DsrA_{34}$ portions in the models, (60 ± 20 Å), is similar to that between the selected models in the EOM ensembles.

be rather limiting for riboregulation during normal growth conditions (52), the biological significance of the observed higher Hfq–RNA complexes remains uncertain. In addition, the studies by Wang *et al.* (13) are at variance with the observations by Updegrove *et al.* (18). Using different experimental approaches, the latter authors showed by mimicking the cellular environment in terms of concentration and ionic strength conditions that Hfq_{Ec} and Hfq_{Ec65} form a 1:1 complex with DsrA or DsrA domain II in solution.

Similarly as observed by Updegrove *et al.* (18), our studies strongly suggest that Hfq_{Ec} and Hfq_{Ec65} form a 1:1 complex with $DsrA_{34}$. Furthermore, the NMR study identified three clusters of residues affected by binding of $DsrA_{34}$ to Hfq_{Ec65}. (i) The YKH motif located in the central pore of the Hfq hexamer together with the surrounding residues residing in the adjacent β-strands. In the YKH motif, K57 and H58 participate in RNA binding in *S. aureus* Hfq (8), whereas Y56 is involved in aromatic stacking interactions stabilizing H58 in an appropriate orientation for interaction with the RNA base. (ii) The N-terminal segment of Hfq, where structuring of aa residues 2–4 was observed. These residues precede the α-helix located on the proximal face of the Hfq hexamer (7) (Figure 1C), and their interaction with RNA might lead to concomitant perturbation of the hydrogen bonding network in the α-helix itself and to some subtle repacking of the α-helix as a whole. (iii) As a consequence, the residues spatially adjacent to the C-cap of the α-helix, i.e. the aa residues 34–37 located at the end of β2-strand and in the turn connecting to the following β2′-strand, are also affected. Although the reason(s) for these chemical shift variations is unclear, it seems possible that this loop has some conformational variability and can assume different conformations in different environments. This hypothesis is supported by our NMR studies as well as by the crystal structure (pdb1HK9 (7)) in that the 34–37 region displays some flexibility, which might result in different conformations and hence in the observed chemical shifts variations in the Hfq_{Ec65}–$DsrA_{34}$ complex. These NMR studies corroborate mutational analyses (9), which likewise indicated that DsrA binds to the proximal site of Hfq.

Biophysical studies (18) have recently shown that a ternary complex between Hfq, DsrA domain II and

polyA$_{18}$, the latter of which was shown to bind to the distal site (11), is rather unstable. However, Soper *et al.* (6) provided evidence that Hfq forms persistent ternary complexes when the two ligands are complemetary. These experiments also indicated that at least transient co-binding between Hfq, *rpoS* mRNA and DsrA contributes to riboregulation, which can be reconciled with the observed rapid binding and release of Hfq from ternary complexes during annealing (21). Hence, the two distinct binding sites on Hfq could at least transiently increase the local concentration of both the sRNA and the mRNA, which could in turn facilitate the interaction of ligands with medium affinities and circumvent the need for a high concentration of either substrate. Taken the above-mentioned studies together with the observation that stable binding of longer mRNAs by Hfq appears to involve contacts with the intrinsically flexible C-termini of Hfq (28,29) and with the structural data presented herein, we suggest the following model for the function of Hfq in riboregulation. The model entails five steps: (i) fast binding of both RNA ligands (21) to Hfq leading to their increased local concentration (Figure 6), followed by (ii) restructuring of the substrates by Hfq (25,26,28). Hereby, the Hfq-induced conformational fluctuations in both the sRNA and mRNA may occur separately. While the intrinsically unstructured region of the C-terminus of Hfq (29) may contribute to mRNA binding and may induce conformational changes in these ligands, it seems to be dispensable for doing so in sRNAs, as the C-terminally truncated Hfq$_{Ec65}$ was proficient to alter the structure of DsrA (28). In addition, at least in the Hfq$_{Ec}$–DsrA$_{34}$ complex, the DsrA$_{34}$ does not interact with the C-terminus of Hfq$_{Ec}$ (Figure 5D–F); (iii) initiation of base-pairing between the ligands (21). In this step, the inherent capacity of Hfq to present RNA in extended conformation and different spatial orientation(s) (Figures 5D–F and 6) would allow to cover a large space over Hfq, which would firstly favour the encounter and secondly the initial annealing of two cognate RNAs. In addition, it has been recently shown that Hfq can bind to the U-rich sequence following the rho-independent terminator of sRNAs (53). Thus, different binding sites of Hfq on one sRNA could be likewise important in terms of increasing the geometric variability of these ligands on the proximal face of Hfq. Moreover, not only the sRNA may be presented in different orientations on the proximal face but—given the presence of six tripartite-binding motifs (11)—also the mRNA bound on the distal side may adopt different orientations. Hence, the geometric variability of the ligands in individual complexes would facilitate annealing in a stochastic manner; (iv) ligand release from Hfq (21,22) followed by (v) stable duplex formation between the RNA substrates. At this juncture, RNA displacement from Hfq may occur by invasion of other RNAs (54). In this model, fast binding, restructuring and the presence of conformationally variable complexes would not only ensure a fast turnover of cognate RNAs but could also provide a means of proofreading for non-cognate ligands, i.e. where initial base pairing cannot take place. Similarly, Doetsch *et al.* (55) suggested that a human immunodeficiency virus-1 derived Tat peptide accelerates annealing of two RNA ligands by changing the population distribution of RNA structures to favour an annealing-competent RNA conformation.

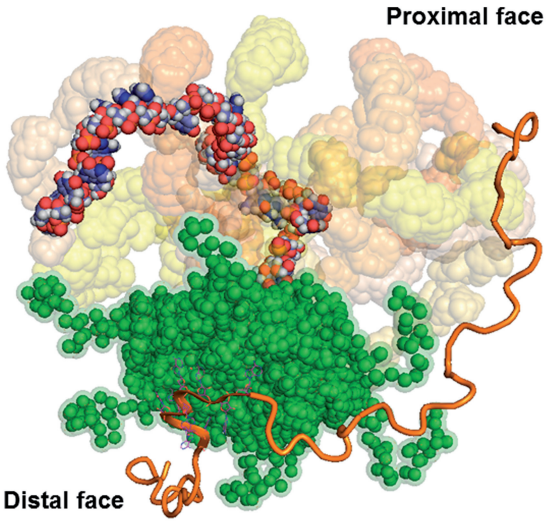

Figure 6. Model of Hfq RNA chaperone function. The sRNA displayed by the full-atom model with atoms colour-coded is shown bound to the proximal face of Hfq$_{Ec}$ (green, solvent accessible surface). Through conformational fluctuations, the sRNA can cover a larger conformational space (nine representative DsrA$_{34}$ models are displayed with their solvent accessible surface coloured as in Figure 5). The mRNA is bound on the distal side (polyA$_9$ orange flat cartoon representation) to one of the six tripartite binding motifs as shown in the crystal structure pdb3GIB (11). The model of a hypothetical mRNA chain is displayed in orange oval cartoon. Hfq$_{Ec}$ acts by restructuring the mRNA (6), which may be accomplished by the conformationally flexible C-termini (29). The structural variability of both RNAs in a transient ternary 1:1:1 complex (18) would allow to sample large spaces. In this way, Hfq$_{Ec}$ would not only act as a platform for binding and by increasing the local concentration of both ligands but would also serve to promote their flexibility and consequently successful annealing in a stochastic manner.

As mentioned above, the increased local concentration of two RNA ligands together with the structural plasticity of RNA bound to the RNA chaperone Hfq would allow the RNA to sample large spaces and therefore enhance the probability of successful annealing between RNAs. This capacity of Hfq appears to be of particular importance when the free energy of sRNA–mRNA pairing interactions is low, i.e. when the complementarity of Hfq-dependent sRNAs and their target mRNAs is non-contiguous, as it is the case for many studied sRNA–mRNA pairs in GC-rich Enterobacteriaceae (56). In contrast, Hfq is dispensable for duplex formation between the sRNA IstR-1 and tisAB mRNA in *E. coli* (57) as well as for base pairing between RNAIII and the target mRNA sa1000 in *S. aureus* (58). In both cases, the free energy of base-pairing is ~2–3-fold higher than observed for Hfq-dependent sRNA–mRNA duplexes in *E. coli*. Experimental support for the link between the Hfq requirement and the free energy of sRNA–mRNA pairing has also been obtained by Woodson *et al.* (21). Overexpression of DsrA resulted in increased *rpoS* translation even in the absence of Hfq, whereas ArcZ and RprA, which are also known to stimulate RpoS synthesis,

were unable to do so. These authors further showed that DsrA binds the *rpoS* leader more tightly in the absence of Hfq than RprA and ArcZ and concluded that the stability of the RNA duplex between *rpoS* mRNA and the sRNA rather than the kinetics of formation is important.

In conclusion, the proposed molecular mechanism for Hfq-mediated RNA annealing is reminiscent of that suggested for intrinsically unstructured proteins and their interactions with protein partners. In these proteins, flexible, intrinsically disordered regions are believed to provide conformational fluctuations, which can facilitate intermolecular interactions, forming complexes with high specificity and relatively low affinity. This is critical for processes in which not only specific association but also subsequent dissociation of binding partners is required (59).

SUPPLEMENTARY DATA

Supplementary Data are available at NAR Online: Supplementary Table 1 and Supplementary Figures 1–3.

ACKNOWLEDGEMENTS

We thank Giuseppe Zaccai (ILL, Grenoble, France) for fruitful discussions. E.d.A.R., K.D.-C., U.B. and M.B.-F. Conceived and designed the experiments: EdAR, MB-F, UB, KDj-C, UB. Performed the experiments: EdAR, HH, GK, BV, MB-F. Analysed the data: EdAR, DS, KDj-C, UB, PK, WS, GK. Wrote the paper: EdAR, KDj-C, UB, DS, PK, WS, GK. Edited the manuscript: HP, DS, UB, KDj-C.

FUNDING

Special Research Program (SFB17) on 'Modulators of RNA fate and function' by the Austrian Science Fund [F1722 to K.D.-C. and F1720 to U.B.]; Bundesministerium für Bildung und Forschung grant SYNC-LIFE [contract number 05K10YEA to D.I.S.]; European Union FP7 e-Infrastructure grant WeNMR [contract number 261572 to D.I.S.]. Funding for open access charge: Austrian Science Fund.

Conflict of interest statement. None declared.

REFERENCES

1. Vogel,J. and Luisi,B.F. (2011) Hfq and its constellation of RNA. *Nat. Rev. Microbiol.*, **9**, 578–589.
2. Zhang,A., Wassarman,K.M., Ortega,J., Steven,A.C. and Storz,G. (2002) The Sm-like Hfq protein increases OxyS RNA interaction with target mRNAs. *Mol. Cell*, **9**, 11–22.
3. Wilusz,C.J. and Wilusz,J. (2005) Eukaryotic Lsm proteins: lessons from bacteria. *Nat. Struct. Mol. Biol.*, **12**, 1031–1036.
4. Repoila,F. and Darfeuille,F. (2009) Small regulatory non-coding RNAs in bacteria: physiology and mechanistic aspects. *Biol. Cell*, **101**, 117–131.
5. Beisel,C.L. and Storz,G. (2010) Base pairing small RNAs and their roles in global regulatory networks. *FEMS Microbiol. Rev.*, **34**, 866–882.
6. Soper,T.J., Doxzen,K. and Woodson,S.A. (2011) Major role for mRNA binding and restructuring in sRNA recruitment by Hfq. *RNA*, **17**, 1544–1550.
7. Sauter,C., Basquin,J. and Suck,D. (2003) Sm-like proteins in eubacteria: the crystal structure of the Hfq protein from *Escherichia coli*. *Nucleic Acids Res.*, **31**, 4091–4098.
8. Schumacher,M.A., Pearson,R.F., Moller,T., Valentin-Hansen,P. and Brennan,R.G. (2002) Structures of the pleiotropic translational regulator Hfq and an Hfq-RNA complex: a bacterial Sm-like protein. *EMBO J.*, **21**, 3546–3556.
9. Mikulecky,P.J., Kaw,M.K., Brescia,C.C., Takach,J.C., Sledjeski,D.D. and Feig,A.L. (2004) *Escherichia coli* Hfq has distinct interaction surfaces for DsrA, rpoS and poly(A) RNAs. *Nat. Struct. Mol. Biol.*, **11**, 1206–1214.
10. Sauer,E. and Weichenrieder,O. (2011) Structural basis for RNA 3′-end recognition by Hfq. *Proc. Natl Acad. Sci. USA*, **108**, 13065–13070.
11. Link,T.M., Valentin-Hansen,P. and Brennan,R.G. (2009) Structure of *Escherichia coli* Hfq bound to polyriboadenylate RNA. *Proc. Natl Acad. Sci. USA*, **106**, 19292–19297.
12. Someya,T., Baba,S., Fujimoto,M., Kawai,G., Kumasaka,T. and Nakamura,K. (2011) Crystal structure of Hfq from *Bacillus subtilis* in complex with SELEX-derived RNA aptamer: insight into RNA-binding properties of bacterial Hfq. *Nucleic Acids Res.*, 1–12.
13. Wang,W., Wang,L., Zou,Y., Zhang,J., Gong,Q., Wu,J. and Shi,Y. (2011) Cooperation of *Escherichia coli* Hfq hexamers in DsrA binding. *Genes Dev.*, **25**, 2106–2117.
14. Lease,R.A., Cusick,M.E. and Belfort,M. (1998) Riboregulation in *Escherichia coli*: DsrA RNA acts by RNA:RNA interactions at multiple loci. *Proc. Natl Acad. Sci. USA*, **95**, 12456–12461.
15. Sledjeski,D.D., Whitman,C. and Zhang,A. (2001) Hfq is necessary for regulation by the untranslated RNA DsrA. *J. Bacteriol.*, **183**, 1997–2005.
16. Resch,A., Večerek,B., Palavra,K. and Bläsi,U. (2010) Requirement of the CsdA DEAD-box helicase for low temperature riboregulation of *rpoS* mRNA. *RNA Biol.*, **7**, 796–802.
17. Resch,A., Afonyushkin,T., Lombo,T.B., McDowall,K.J., Bläsi,U. and Kaberdin,V.R. (2008) Translational activation by the noncoding RNA DsrA involves alternative RNase III processing in the rpoS 5′-leader. *RNA*, **14**, 454–459.
18. Updegrove,T.B., Correia,J.J., Chen,Y., Terry,C. and Wartell,R.M. (2011) The stoichiometry of the *Escherichia coli* Hfq protein bound to RNA. *RNA*, **17**, 489–500.
19. Soper,T.J. and Woodson,S.A. (2008) The rpoS mRNA leader recruits Hfq to facilitate annealing with DsrA sRNA. *RNA*, **14**, 1907–1917.
20. Soper,T., Mandin,P., Majdalani,N., Gottesman,S. and Woodson,S.A. (2010) Positive regulation by small RNAs and the role of Hfq. *Proc. Natl Acad. Sci. USA*, **107**, 9602–9607.
21. Woodson,S.A., Hopkins,J.F. and Panja,S. (2011) Rapid binding and release of Hfq from ternary complexes during RNA annealing. *Nucleic Acids Res.*, **39**, 5193–5202.
22. Lease,R.A. and Woodson,S.A. (2004) Cycling of the Sm-like protein Hfq on the DsrA small regulatory RNA. *J. Mol. Biol.*, **344**, 1211–1223.
23. Brescia,C.C., Mikulecky,P.J., Feig,A.L. and Sledjeski,D.D. (2003) Identification of the Hfq-binding site on DsrA RNA: Hfq binds without altering DsrA secondary structure. *RNA*, **9**, 33–43.
24. Majdalani,N., Cunning,C., Sledjeski,D., Elliott,T. and Gottesman,S. (1998) DsrA RNA regulates translation of RpoS message by an anti-antisense mechanism, independent of its action as an antisilencer of transcription. *Proc. Natl Acad. Sci. USA*, **95**, 12462–12467.
25. Moll,I., Leitsch,D., Steinhauser,T. and Bläsi,U. (2003) RNA chaperone activity of the Sm-like Hfq protein. *EMBO Rep.*, **4**, 284–289.
26. Geissmann,T.A. and Touati,D. (2004) Hfq, a new chaperoning role: binding to messenger RNA determines access for small RNA regulator. *EMBO J.*, **23**, 396–405.
27. Udekwu,K.I., Darfeuille,F., Vogel,J., Reimegard,J., Holmqvist,E. and Wagner,E.G.H. (2005) Hfq-dependent regulation of OmpA synthesis is mediated by an antisense RNA. *Genes Dev.*, **19**, 2355–2366.

28. Večerek,B., Rajkowitsch,L., Sonnleitner,E., Schroeder,R. and Bläsi,U. (2008) The C-terminal domain of *Escherichia coli* Hfq is required for regulation. *Nucleic Acids Res.*, **36**, 133–143.
29. Beich-Frandsen,M., Večerek,B., Konarev,P.V., Sjoblom,B., Kloiber,K., Hammerle,H., Rajkowitsch,L., Miles,A.J., Kontaxis,G., Wallace,B.A. *et al.* (2011) Structural insights into the dynamics and function of the C-terminus of the *E. coli* RNA chaperone Hfq. *Nucleic Acids Res.*, **39**, 4900–4915.
30. Garcia De La Torre,J., Huertas,M.L. and Carrasco,B. (2000) Calculation of hydrodynamic properties of globular proteins from their atomic-level structure. *Biophys. J.*, **78**, 719–730.
31. Delaglio,F., Grzesiek,S., Vuister,G.W., Zhu,G., Pfeifer,J. and Bax,A. (1995) NMRPipe: a multidimensional spectral processing system based on UNIX pipes. *J. Biomol. NMR*, **6**, 277–293.
32. Goddard,T.D. and Kneller,D.G. Sparky—NMR Assignment and Integration Software. University of California, San Francisco, CA.
33. Piotto,M., Saudek,V. and Sklenar,V. (1992) Gradient-tailored excitation for single-quantum NMR spectroscopy of aqueous solutions. *J. Biomol. NMR*, **2**, 661–665.
34. Kay,L.E., Ikura,M., Tschudin,R. and Bax,A. (1990) Three-dimensional triple-resonance NMR spectroscopy of isotopically enriched proteins. *J. Magn. Reson.*, **89**, 496–514.
35. Bax,A. and Ikura,M. (1991) An efficient 3D NMR technique for correlating the proton and 15N backbone amide resonances with the alpha-carbon of the preceding residue in uniformly 15N/13C enriched proteins. *J. Biomol. NMR*, **1**, 99–104.
36. Wittekind,M. and Mueller,L. (1993) HNCACB, a high-sensitivity 3D NMR experiment to correlate amide-proton and nitrogen resonances with the alpha- and beta-carbon resonances in proteins. *J. Magn. Reson.*, **101**, 201–205.
37. Farrow,N.A., Muhandiram,R., Singer,A.U., Pascal,S.M., Kay,C.M., Gish,G., Shoelson,S.E., Pawson,T., Forman-Kay,J.D. and Kay,L.E. (1994) Backbone dynamics of a free and phosphopeptide-complexed Src homology 2 domain studied by 15N NMR relaxation. *Biochemistry*, **33**, 5984–6003.
38. Farrow,N.A., Zhang,O., Szabo,A., Torchia,D.A. and Kay,L.E. (1995) Spectral density function mapping using 15N relaxation data exclusively. *J. Biomol. NMR*, **6**, 153–162.
39. Roessle,M.W., Klaering,R., Ristau,U., Robrahn,B., Jahn,D., Gehrmann,T., Konarev,P., Round,A., Fiedler,S., Hermes,C. *et al.* (2007) Upgrade of the small-angle X-ray scattering beamline X33 at the European Molecular Biology Laboratory, Hamburg. *J. Appl. Crystallogr.*, **40**, S190–S194.
40. Roessle,M., Round,A.R., Franke,D., Moritz,S., Huchler,R., Fritsche,M., Malthan,D., Klaering,R. and Svergun,D.I. (2008) Automated sample-changing robot for solution scattering experiments at the EMBL Hamburg SAXS station X33. *J. Appl. Crystallogr.*, **41**, 913–917.
41. Konarev,P.V., Petoukhov,M.V., Volkov,V.V. and Svergun,D.I. (2006) ATSAS 2.1, a program package for small-angle scattering data analysis. *J. Appl. Crystallogr.*, **39**, 277–286.
42. Konarev,P.V., Volkov,V.V., Sokolova,A.V., Koch,M.H.J. and Svergun,D.I. (2003) PRIMUS: a Windows PC-based system for small-angle scattering data analysis. *J. Appl. Crystallogr.*, **36**, 1277–1282.
43. Svergun,D.I. (1992) Determination of the regularization parameter in indirect-transform methods using perceptual criteria. *J. Appl. Crystallogr.*, **25**, 495–503.
44. Svergun,D.I. (1999) Restoring low resolution structure of biological macromolecules from solution scattering using simulated annealing. *Biophys. J.*, **76**, 2879–2886.
45. Bernado,P., Mylonas,E., Petoukhov,M.V., Blackledge,M. and Svergun,D.I. (2007) Structural characterization of flexible proteins using small-angle X-ray scattering. *J. Am. Chem. Soc.*, **129**, 5656–5664.
46. Petoukhov,M.V. and Svergun,D.I. (2005) Global rigid body modeling of macromolecular complexes against small-angle scattering data. *Biophys. J.*, **89**, 1237–1250.
47. Flores,S.C., Wan,Y., Russell,R. and Altman,R.B. (2010) Predicting RNA structure by multiple template homology modeling. *Pac. Symp. Biocomput.*, 216–227.
48. Flores,S.C. and Altman,R.B. (2010) Turning limited experimental information into 3D models of RNA. *RNA*, **16**, 1769–1778.
49. Caliskan,G., Hyeon,C., Perez-Salas,U., Briber,R.M., Woodson,S.A. and Thirumalai,D. (2005) Persistence length changes dramatically as RNA folds. *Phys. Rev. Lett.*, **95**, 268303.
50. Hyeon,C., Dima,R.I. and Thirumalai,D. (2006) Size, shape, and flexibility of RNA structures. *J. Chem. Phys.*, **125**, 194905.
51. Sun,X. and Wartell,R.M. (2006) *Escherichia coli* Hfq binds A18 and DsrA domain II with similar 2:1 Hfq6/RNA stoichiometry using different surface sites. *Biochemistry*, **45**, 4875–4887.
52. Moon,K. and Gottesman,S. (2011) Competition among Hfq-binding small RNAs in *Escherichia coli*. *Mol. Microbiol.*, **82**, 1545–1562.
53. Otaka,H., Ishikawa,H., Morita,T. and Aiba,H. (2011) PolyU tail of rho-independent terminator of bacterial small RNAs is essential for Hfq action. *Proc. Natl Acad. Sci. USA*, **108**, 13059–13064.
54. Fender,A., Elf,J., Hampel,K., Zimmermann,B. and Wagner,E.G.H. (2010) RNAs actively cycle on the Sm-like protein Hfq. *Genes Dev.*, **24**, 2621–2626.
55. Doetsch,M., Furtig,B., Gstrein,T., Stampfl,S. and Schroeder,R. (2011) The RNA annealing mechanism of the HIV-1 Tat peptide: conversion of the RNA into an annealing-competent conformation. *Nucleic Acids Res.*, **39**, 4405–4418.
56. Jousselin,A., Metzinger,L. and Felden,B. (2009) On the facultative requirement of the bacterial RNA chaperone, Hfq. *Trends Microbiol.*, **17**, 399–405.
57. Darfeuille,F., Unoson,C., Vogel,J. and Wagner,E.G.H. (2007) An antisense RNA inhibits translation by competing with standby ribosomes. *Mol. Cell*, **26**, 381–392.
58. Boisset,S., Geissmann,T., Huntzinger,E., Fechter,P., Bendridi,N., Possedko,M., Chevalier,C., Helfer,A.C., Benito,Y., Jacquier,A. *et al.* (2007) *Staphylococcus aureus* RNAIII coordinately represses the synthesis of virulence factors and the transcription regulator Rot by an antisense mechanism. *Genes Dev.*, **21**, 1353–1366.
59. Tompa,P. and Csermely,P. (2004) The role of structural disorder in the function of RNA and protein chaperones. *FASEB J.*, **18**, 1169–1175.